

# Plasmonic Nanocavity Modes: From Near-Field to Far-Field Radiation

Nuttawut Kongsuwan, Angela Demetriadou, Matthew Horton, Rohit Chikkaraddy, Jeremy J. Baumberg,\* and Ortwin Hess\*



Cite This: <https://dx.doi.org/10.1021/acsp Photonics.9b01445>



Read Online

ACCESS |



Metrics & More



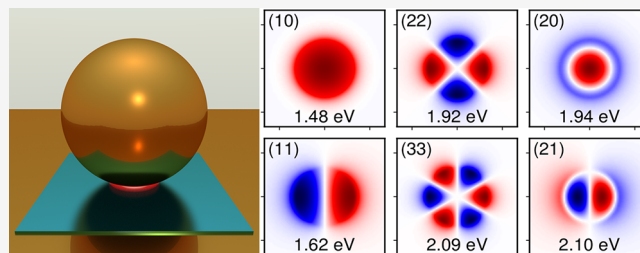
Article Recommendations



Supporting Information

**ABSTRACT:** In the past decade, advances in nanotechnology have led to the development of plasmonic nanocavities that facilitate light–matter strong coupling in ambient conditions. The most robust example is the nanoparticle-on-mirror (NPoM) structure whose geometry is controlled with subnanometer precision. The excited plasmons in such nanocavities are extremely sensitive to the exact morphology of the nanocavity, giving rise to unexpected optical behaviors. So far, most theoretical and experimental studies on such nanocavities have been based solely on their scattering and absorption properties. However, these methods do not provide a complete optical description of the nanocavities. Here, the NPoM is treated as an open nonconservative system supporting a set of photonic quasinormal modes (QNMs). By investigating the morphology-dependent optical properties of nanocavities, we propose a simple yet comprehensive nomenclature based on spherical harmonics and report spectrally overlapping bright and dark nanogap eigenmodes. The near-field and far-field optical properties of NPoMs are explored and reveal intricate multimodal interactions.

**KEYWORDS:** plasmonics, nanophotonics, nanocavities, quasinormal mode, near-to-far-field transformation



Metallic nanostructures have the ability to confine light below the diffraction limit via the collective excitation of conduction electrons, called localized surface plasmons. Through recent advances in nanofabrication techniques, gaps of just 1–2 nm between nanostructures have been achieved.<sup>1,2</sup> At such extreme nanogaps, the plasmonic modes of two nanostructures hybridize to allow an unprecedented light confinement,<sup>3,4</sup> making coupled nanostructures an ideal platform for field-enhanced spectroscopy,<sup>5,6</sup> photocatalysis,<sup>7</sup> and nano-optoelectronics.<sup>8</sup> One such nanostructure is the nanoparticle-on-mirror (NPoM) geometry, where a nanoparticle is separated from an underlying metal film by a molecular monolayer.<sup>9,10</sup> This geometry (which resembles the prototypical dimer, but is more reliable and robust to fabricate) has attracted considerable interest since it enables light–matter strong-coupling of a single molecule at room temperature,<sup>11</sup> and it has many potential applications, including biosensing<sup>12</sup> and quantum information.<sup>13,14</sup>

A wide range of theoretical and experimental studies have been conducted to investigate the optical properties of NPoM nanocavities.<sup>12,15,16</sup> Several studies examine resonances of NPoMs<sup>17–21</sup> and their influence on optical emission of single molecules in the nanogaps.<sup>22–24</sup> However, only a few studies to date analyze the inherent resonant states of the NPoM nanocavities,<sup>25–27</sup> and most other studies have so far described their optical responses via a scattering method, inferring their

resonances from far-field spectral peaks. Although significant information can be obtained from the far-field spectra, they do not reveal complete optical descriptions of the nanocavities and commonly hide information about their dark modes. For example, an incident field from the far-field does not couple to all available photonic modes of the system. Resonances that are spectrally close also interfere with each other and often merge into single broadened peaks in far-field spectra. As a result, analyses of the far-field scattered spectra can yield inconsistencies between near-field and far-field plasmonic responses.<sup>28</sup>

The precise morphological details of the NPoM nanogaps also dramatically modify their optical response.<sup>17,29</sup> Once the nanoparticles are placed on substrates, they lie on their facets, which can have varying facet widths. Previous studies of the gap morphology of NPoMs described their gap plasmonic resonances with two sets of modes: longitudinal antenna modes, excited for all facet widths, and transverse waveguide modes, excited at large facet widths.<sup>18,19</sup> Although this description sheds light on the asymptotic behavior of the

Received: October 5, 2019

Published: January 9, 2020

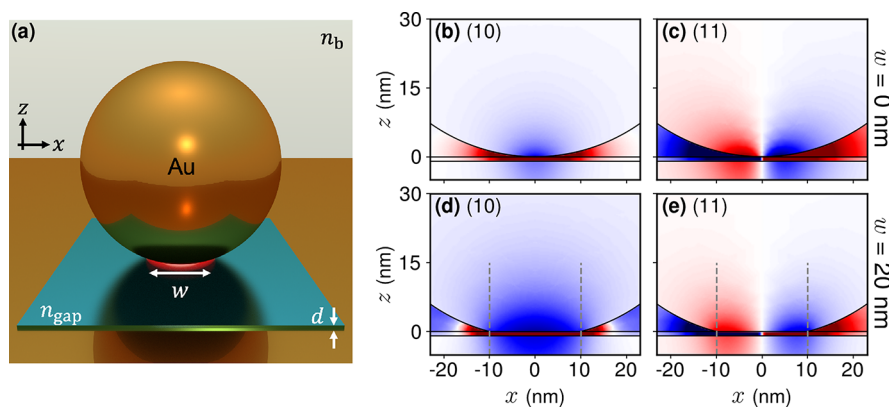


**Figure 1.** (a) Schematic for a gold nanoparticle-on-mirror (NPOM) structure with the diameter  $2R = 80$  nm, nanogap  $d = 1$  nm, nanogap index  $n_{\text{gap}} = 1.45$ , background index  $n_b = 1$ , and facet width  $w$ . (b, c, d, e) Normalized quasinormal-mode (QNM) electric fields  $E_{z,lm}$  in the vertical  $xz$ -plane of NPOMs with (b, c)  $w = 0$  and (d, e)  $w = 20$  nm for (b, d) the (10) mode and (c, e) the (11) mode. The gray dashed lines indicate the facet edges.

NPOM plasmons, it provides an incomplete picture of NPOM resonances at intermediate facet widths.

In this Article, we identify and map the inherent resonant states of the NPOM geometry by employing the quasinormal mode (QNM) method.<sup>30</sup> We propose a simple yet comprehensive nomenclature based on spherical harmonics to describe the resonances of NPOMs with varying morphologies. A collection of spectrally overlapping bright and dark nanogap QNMs are reported, including some photonic modes that have not been reported elsewhere. These results imply that a quantum emitter placed inside a NPOM nanogap couples to a collection of QNMs and experiences a complex multimodal interaction. By calculating the far-field emission of each QNM using a near-to-far-field transformation (NFFT) method, we predict the total emission profile of a dipole emitter placed inside a NPOM nanogap from the QNM collective responses. The resulting emission profiles display rich and intricate behaviors, governed by the NPOM morphology.

**Eigenmodes of Plasmonic Nanocavities.** A general open system is nonconservative as its energy leaks to its surrounding environment, and therefore, its time-evolution is non-Hermitian. Consequently, its resonances can no longer be described by normal modes but instead are characterized by QNMs with complex eigenfrequencies.<sup>31</sup> The QNM analysis is a standard methodology to study open and dissipative systems, of which the approximate descriptions are often provided by a few QNMs. This approach has spanned a wide range of applications, including gravitational waves from black holes<sup>32</sup> and electromagnetic waves from nanoresonators.<sup>30</sup>

In nanophotonics, significant progress has been made in the past decades toward solving QNMs for general dispersive materials. Efficient QNM solvers have been developed using a variety of techniques, including the time-domain approach,<sup>33,34</sup> the pole-search approach,<sup>35–37</sup> and the auxiliary-field eigenvalue approach.<sup>27</sup> For resonators with arbitrary shapes and materials, analytic solutions are not generally available, and several numerical methods have been developed that surround the resonators by perfectly matched layers (PMLs) to approximately simulate infinite domains.<sup>27,38</sup>

Here, we represent the resonances as QNMs with complex frequencies  $\tilde{\omega}_i = \omega_i - i\kappa_i$ , where the real part,  $\omega_i$ , is the spectral position and the imaginary part,  $\kappa_i$ , is the line width, that is, the dissipation rate. For a general optical system with nonmagnetic

materials, its QNMs can be found by solving the time-harmonic and source-free Maxwell's equations<sup>30</sup>

$$\begin{pmatrix} 0 & -i\mu_0^{-1}\nabla\times \\ i\epsilon(\mathbf{r};\tilde{\omega}_i)^{-1}\nabla\times & 0 \end{pmatrix} \begin{pmatrix} \tilde{\mathbf{H}}_i(\mathbf{r}) \\ \tilde{\mathbf{E}}_i(\mathbf{r}) \end{pmatrix} = \tilde{\omega}_i \begin{pmatrix} \tilde{\mathbf{H}}_i(\mathbf{r}) \\ \tilde{\mathbf{E}}_i(\mathbf{r}) \end{pmatrix} \quad (1)$$

where  $\epsilon(\mathbf{r};\tilde{\omega}_i)$  is the permittivity and  $\tilde{\mathbf{H}}_i$  and  $\tilde{\mathbf{E}}_i$  are the magnetic and electric fields of a QNM that satisfy the Sommerfeld radiation condition for outgoing waves.

For dispersive materials like metals, eq 1 is, in general, a nonlinear eigenvalue equation. However, eq 1 can be converted into a linear equation if the material permittivities are described by an  $N$ -pole Lorentz–Drude permittivity

$$\epsilon(\omega) = \epsilon_\infty \left( 1 - \sum_{k=1}^N \frac{\omega_{p,k}^2}{\omega^2 - \omega_{0,k}^2 + i\gamma_k\omega} \right) \quad (2)$$

where  $\epsilon_\infty$  is the asymptotic permittivity at infinite frequency, while  $\omega_{p,k}$ ,  $\omega_{0,k}$ , and  $\gamma_k$  are the plasma frequency, resonant frequency, and decay rate, respectively, of the  $k^{\text{th}}$  Lorentz–Drude pole. For each Lorentz–Drude pole in the summation, two auxiliary fields can be introduced<sup>27</sup>

$$\tilde{\mathbf{P}}_{i,k}(\mathbf{r}) = -\frac{\epsilon_\infty\omega_{p,k}^2}{\tilde{\omega}_i^2 - \omega_{0,k}^2 + i\gamma_k\tilde{\omega}_i} \tilde{\mathbf{E}}_i(\mathbf{r}) \quad (3)$$

$$\tilde{\mathbf{J}}_{i,k}(\mathbf{r}) = -i\tilde{\omega}_i\tilde{\mathbf{P}}_{i,k}(\mathbf{r}) \quad (4)$$

where  $\tilde{\mathbf{P}}_{i,k}$  and  $\tilde{\mathbf{J}}_{i,k}$  are auxiliary polarization and current, respectively, of the  $i^{\text{th}}$  QNM and the  $k^{\text{th}}$  Lorentz–Drude pole. In the case of a single pole permittivity ( $N = 1$ ), the auxiliary fields can be inserted into eq 1 to obtain a linear eigenvalue equation

$$\hat{\mathcal{H}}\tilde{\psi}_i = \tilde{\omega}_i\tilde{\psi}_i \quad (5)$$

$$\tilde{\psi}_i = (\tilde{\mathbf{H}}_i(\mathbf{r}) \tilde{\mathbf{E}}_i(\mathbf{r}) \tilde{\mathbf{P}}_i(\mathbf{r}) \tilde{\mathbf{J}}_i(\mathbf{r}))^T \quad (6)$$

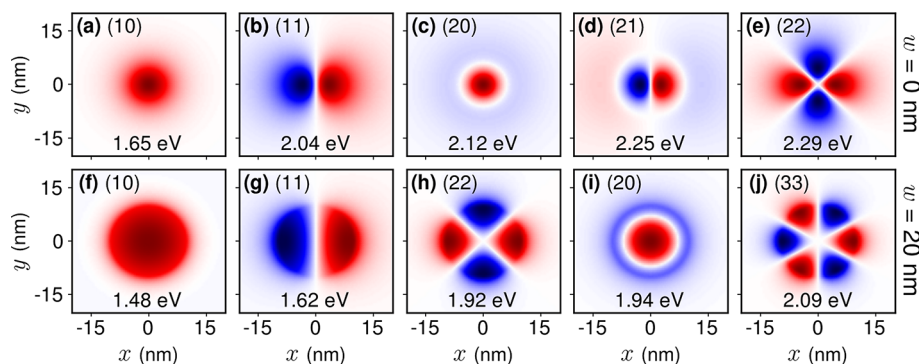


**Figure 2.** Normalized QNM electric fields  $E_{z,lm}$  in the horizontal  $xy$ -plane at the nanogap center for the first five QNMs of NPoMs with (a–e)  $w = 0$  nm and (f–j)  $w = 20$  nm. The real eigenfrequencies  $\omega_{lm}$  in eV are shown at the bottom of all panels.

$$\hat{\mathcal{H}} = \begin{pmatrix} 0 & -i\mu_0^{-1}\nabla\times & 0 & 0 \\ i\epsilon_\infty^{-1}\nabla\times & 0 & 0 & -i\epsilon_\infty^{-1} \\ 0 & 0 & 0 & i \\ 0 & i\omega_p^2\epsilon_\infty & -i\omega_p^2 & -i\gamma \end{pmatrix} \quad (7)$$

The treatment of gold permittivity is given in section S1.1 in Supporting Information.

Unlike real-frequency normal modes, the QNMs have unique properties such that their fields diverge in space at a large distance. Hence, the QNMs do not have finite energy and cannot be normalized based on energy considerations.<sup>30</sup> The orthogonality relation and normalization of the QNMs take the following form<sup>27</sup>

$$\iiint_{\Omega} \left[ \epsilon_\infty \tilde{\mathbf{E}}_i \cdot \tilde{\mathbf{E}}_j - \mu_0 \tilde{\mathbf{H}}_i \cdot \tilde{\mathbf{H}}_j + \frac{\omega_0^2}{\epsilon_\infty \omega_p^2} \tilde{\mathbf{P}}_i \cdot \tilde{\mathbf{P}}_j - \frac{1}{\epsilon_\infty \omega_p^2} \tilde{\mathbf{J}}_i \cdot \tilde{\mathbf{J}}_j \right] d^3\mathbf{r} = \delta_{ij} \quad (8)$$

where  $\delta_{ij} = 1$  if  $i = j$  and 0 otherwise. The integration domain  $\Omega$  must include both the system and the PMLs.

To calculate the QNMs of a gold NPoM structure, we employ the above methodology by using QNMEig, an open-source program based on COMSOL Multiphysics, which implements an efficient finite-element solver by accounting for material dispersion with auxiliary fields.<sup>27</sup> The parameters are chosen based on recent experiments,<sup>11,17</sup> with a nanoparticle diameter of  $2R = 80$  nm, gap thickness  $d = 1$  nm, refractive index  $n_{\text{gap}} = 1.45$ , and background refractive index  $n_b = 1.0$ , as shown in Figure 1a.

Here, we introduce a comprehensive nomenclature based on spherical harmonics  $Y_l^m$ . Each QNM is labeled with  $i = (lm)$ , where  $l = 1, 2, 3, \dots$  and  $-l \leq m \leq l$ . For an isolated spherical nanoparticle, spherical harmonics form a complete set of orthogonal basis functions for its plasmonic modes. For a NPoM with a spherical nanoparticle, these plasmonic modes are coupled to their image charges in the mirror and become densely distributed near the gap, forming gap plasmons. We report here that the gap plasmons in the nanocavity preserve the nomenclature of plasmons of an isolated nanoparticle despite the fact that the actual plasmons are highly deformed by the mirror. Unlike the previous description by Tserkezis et al.,<sup>18</sup> which categorizes the NPoMs' QNMs into longitudinal antenna modes (valid for all facet widths) and transverse waveguide modes (valid at large facet widths), the proposed nomenclature provides a simpler and more comprehensive

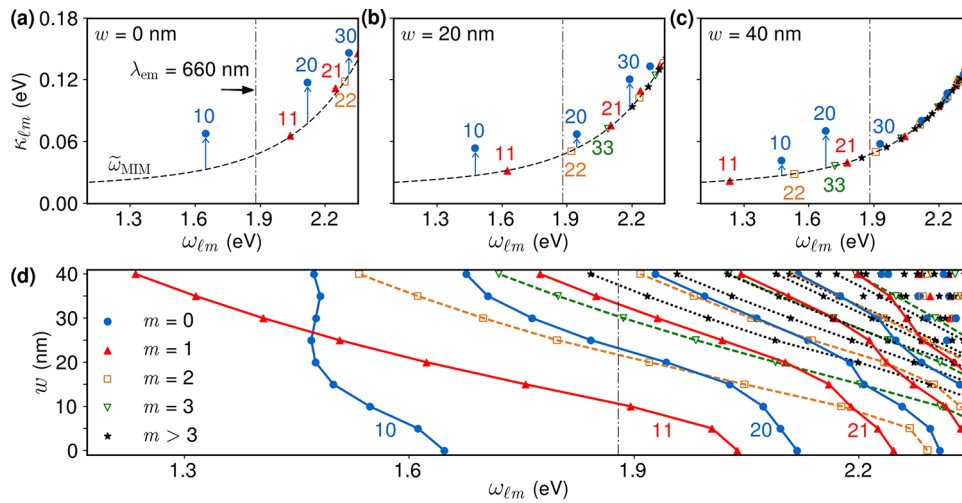
description, based on mode symmetries, which is valid for all facet widths.

Figure 1b,c shows the real  $z$ -component of QNM fields  $E_{z,lm} = \text{Re}[\tilde{\mathbf{E}}_{lm} \cdot \hat{\mathbf{e}}_z]$  for the two lowest-eigenfrequency QNMs, denoted as (10) and (11), of a spherical NPoM ( $w = 0$  nm). At the nanogap, these QNMs exhibit large field confinement far below the diffraction limit, which is the main characteristic of gap plasmons. The (10) mode, also commonly referred to as the bonding dipole plasmon, is symmetric (even) across the  $x = 0$  plane, whereas the (11) mode is antisymmetric (odd), which also encodes their bright and dark natures, respectively. Note that for electromagnetic problems, the (00) mode is undetermined and does not contribute to the fields.<sup>39,40</sup>

Figure 2a–e further explores the field profiles of the first five QNMs in the spherical NPoM nanogap, where the label ( $lm$ ) is assigned to each QNM according to its symmetries. The label  $l$  determines the number of nodes and antinodes along the radial coordinates  $r = \sqrt{x^2 + y^2}$ , whereas the label  $m$  directly corresponds to the number of antinode pairs along the angular coordinate  $\phi = \arctan(y/x)$ , with  $\tilde{\mathbf{E}}_{lm}(r, \phi, z) \propto \exp(im\phi)$ . The ( $l0$ ) modes have a circular symmetry. They also display antinodes at the center  $r = 0$  and  $l - 1$  nodes along  $r$ . On the other hand, the QNMs with  $m \neq 0$  have nodes at the center, which extend radially at angles  $(2n + 1)\pi/2m$  for  $n \in \mathbb{Z}$ . For a given  $m \neq 0$ , each QNM with  $l = |m|$  has only one node at the center, and each successive increment in  $l$  gives one more node along  $r$ , as shown in Figure 2b,d,e. Here, the QNMs with negative  $m = -|m|$  are omitted since they are degenerate with those of the same  $l$  but with positive  $m = +|m|$ . The field profile of the degenerate pair of each QNM can be easily obtained by rotating its fields by angle  $\pi/2m$  around the  $z$ -axis.

Following this nomenclature, our calculations show that the first 20 QNMs of the spherical NPoM ( $w = 0$  nm), arranged in order of ascending real eigenfrequencies, are ( $lm$ ) = (10), (11), (20), (21), (22), (30), (31), (32), (33), (40), (41), (42), (43), (50), (44), (51), (52), (53), (60), and (54), respectively. The results demonstrate two key features: (i) modes of the same  $l$  have higher eigenfrequencies with increasing  $|m|$ , (ii) the first 13 QNMs with different  $l$  values do not spectrally overlap (see Figure S3 in the Supporting Information).

**Faceted Nanocavities.** Real metal nanoparticles are always faceted and lie on their facets with varying widths on a substrate.<sup>17,29</sup> Since the gap plasmonic resonances are highly sensitive to the gap morphology, the gold nanoparticles are modeled as truncated spheres with facet widths  $w$  from 0 to 40



**Figure 3.** Complex eigenfrequencies  $\tilde{\omega}_{lm} = \omega_{lm} - i\kappa_{lm}$  of NPoMs with facet widths (a)  $w = 0$ , (b) 20, and (c) 40 nm. The QNMs with  $|m| = 0, 1, 2$ , and 3 are shown as blue circles, red triangles, orange squares, and green inverted triangles, respectively, whereas  $|m| > 3$  QNMs are shown as black stars. The dashed lines correspond to the complex eigenfrequencies  $\tilde{\omega}_{\text{MIM}}$  of the MIM plasmonic waveguide, whereas the dash-dotted vertical lines indicate the emitter wavelength  $\lambda_{\text{em}} = 660$  nm (1.88 eV), which is considered in Figures 6 and 7. The blue arrows indicate the radiative ( $l0$ ) modes. (d) The real eigenfrequencies  $\omega_i$  for  $w = 0$ –40 nm. The fitted lines connect the QNMs with the same labels.

nm. The remaining nanoparticle facets outside the gap region do not play any significant role. We confirm that the nomenclature defined above is still preserved for faceted NPoMs although their resonant frequencies and optical properties are modified.

As the facet width increases, the optical environment at the nanogap approaches that of a plasmonic waveguide at large facet width. As a result, the QNMs with different  $l$  values become spectrally overlapped because the QNMs, which are more waveguide-like, that is, those with larger  $|m|$ , become more energetically favorable and tend to lie at lower eigenfrequencies.<sup>18</sup> For example, the first 20 QNMs of a faceted NPoM with  $w = 20$  nm are  $(lm) = (10), (11), (22), (20), (33), (21), (30), (44), (32), (31), (55), (40), (43), (66), (41), (42), (54), (77), (50),$  and  $(51)$ , respectively (Figure S3 in the Supporting Information illustrates this spectral overlap). The full list of the QNMs of NPoMs with  $w = 0$ –40 nm is shown in Table S1 in the Supporting Information. As the facet width increases from 0 to 20 nm, the field confinement becomes spread across the facet, as shown in Figures 1d,e and 2f–j for the  $w = 20$  nm NPoM. Nonetheless, the symmetries of these QNMs are preserved for all facet widths, validating the nomenclature used in this article.

Previous studies where the far-field spectra of NPoMs were analyzed<sup>17–19,21</sup> have identified only the ( $l0$ ) and ( $l1$ ) modes. The ( $l0$ ) modes are bright and can be efficiently excited by the vertical ( $z$ -axis) component of a high angle-of-incidence exciting plane wave. The ( $l1$ ) modes, though much darker than the ( $l0$ ), can be efficiently excited on NPoMs with either a horizontally polarized wave plane or two vertically polarized out-of-phase plane waves propagating along opposite directions.<sup>20</sup> On the other hand, higher-order QNMs with  $|m| > 1$ , such as (22) and (33), have not been reported in the literature before. These higher-order QNMs can not be easily isolated since they are very weakly coupled to external fields and spectrally overlap with each other. Hence, they are hidden in far-field spectra and have so far been mostly neglected. However, when a quantum emitter is placed in the plasmonic nanocavity, these dark modes (which can be excited by an emitter's near-field emission) cycle the energy back to the

emitter which in turn excites the bright modes. This phenomenon is insignificant in the weak coupling regime. In the strong-coupling regime,<sup>11</sup> on the other hand, the plexciton-mediated interaction between bright and dark modes can drastically change the energy exchange dynamics and influence the far-field spectra observed.<sup>20</sup>

In order to understand the optical behaviors of gap plasmonic resonances created by faceted NPoM cavities, it is useful to consider the high-order gap plasmonic resonances in the infinite frequency limit  $\omega_{lm} \rightarrow \infty$ , that is,  $\lambda_{lm} \rightarrow 0$ . In this limit, the resonances no longer see the nanoparticle, and the system can simply be treated as a metal–insulator–metal (MIM) plasmonic waveguide.<sup>18,41</sup> The complex eigenfrequencies of the waveguide  $\tilde{\omega}_{\text{MIM}} = \omega_{\text{MIM}} - i\kappa_{\text{MIM}}$  can be calculated by solving the semianalytical parametric equation<sup>16,42</sup>

$$\tanh(d\sqrt{\beta^2 - (\tilde{\omega}_{\text{MIM}}/c)^2\epsilon_{\text{gap}}}) = -\frac{\epsilon_{\text{gap}}\sqrt{\beta^2 - (\tilde{\omega}_{\text{MIM}}/c)^2\epsilon_{\text{Au}}}(\tilde{\omega}_{\text{MIM}})}{\epsilon_{\text{Au}}(\tilde{\omega}_{\text{MIM}})\sqrt{\beta^2 - (\tilde{\omega}_{\text{MIM}}/c)^2\epsilon_{\text{gap}}}} \quad (9)$$

subject to the wave vector parameter  $\beta$  while  $d = 1$  nm is the gap thickness,  $\epsilon_{\text{gap}} = n_{\text{gap}}^2$  is the gap permittivity and  $\epsilon_{\text{Au}}(\tilde{\omega})$  is the gold permittivity. We note that the MIM plasmonic waveguide also has another set of solutions with the opposite parity to eq 9. However, these solutions have zero  $E_z$  field components at the gap center and do not correspond to gap plasmons.

Figure 3a–c investigates the spectral correlations between the QNMs in the complex eigenfrequency plane. We plot with a dashed line the solution of eq 9, which corresponds to the waveguide eigenfrequencies  $\tilde{\omega}_{\text{MIM}}$  as well as the resonant frequencies  $\tilde{\omega}_{lm}$  of the NPoMs. For all facet widths, all QNMs with  $|m| > 0$  lie close to the dashed line of  $\tilde{\omega}_{lm}$ . As  $w$  increases, the QNMs with  $|m| > 0$  simply migrate along  $\tilde{\omega}_{\text{MIM}}$  to lower real-eigenfrequencies. Since the imaginary eigenfrequencies  $\kappa_{lm}$  represent the energy dissipation of the QNMs, these results demonstrate that those with  $\tilde{\omega}_{lm}$  lying along  $\tilde{\omega}_{\text{MIM}}$  are dark modes, and their energies are dissipated almost exclusively through heat at the rate  $\kappa_{\text{MIM}}$ . Only the ( $l0$ ) modes are efficiently radiative and lie significantly above  $\tilde{\omega}_{\text{MIM}}$  because

their charge distributions have nonzero electric dipole moments and are therefore unlike the modes predicted by the MIM model. This implies that the differences between  $\kappa_{l0}$  and  $\kappa_{\text{MIM}}$  correspond to energy dissipation through far-field radiation (shown as blue arrows in Figure 3a–c).

To visualize how the QNMs evolve with varying facet width  $w$ , Figure 3d plots real eigenfrequencies  $\omega_{lm}$  of all QNMs of NPoMs with facet widths  $w$  between 0 and 40 nm. Most QNMs red-shift with increasing  $w$ . There are a few exceptions, such as the (10) modes, which start at  $w = 0$  nm as the lowest eigenfrequency QNM and then level off beyond  $w > 25$  nm. The QNMs with larger  $|m|$  generally red-shift at more rapid rates. For example, the (11) mode appears at lower frequency than the (10) mode for facet sizes around  $w = 25$  nm, and the (22) mode becomes more energetically favorable than the (21) and (20) modes for facet sizes  $w = 10$  and 15 nm, respectively. These results demonstrate complicated spectral relations between bright and dark resonances of NPoMs with different facet widths, leading to vastly different near- and far-field optical behaviors.

To further explore the radiative nature of each QNM, we estimate the radiation efficiency of the ( $lm$ ) mode as

$$\eta_{lm} = \frac{\kappa_{lm} - \kappa_{\text{MIM}}}{\kappa_{lm}} = 1 - \frac{\kappa_{\text{MIM}}}{\kappa_{lm}} \quad (10)$$

Figure 4 shows the radiation efficiencies of (10), (20), (30), (40), (11), (21), (31), (41), (22), and (33) modes. Overall,

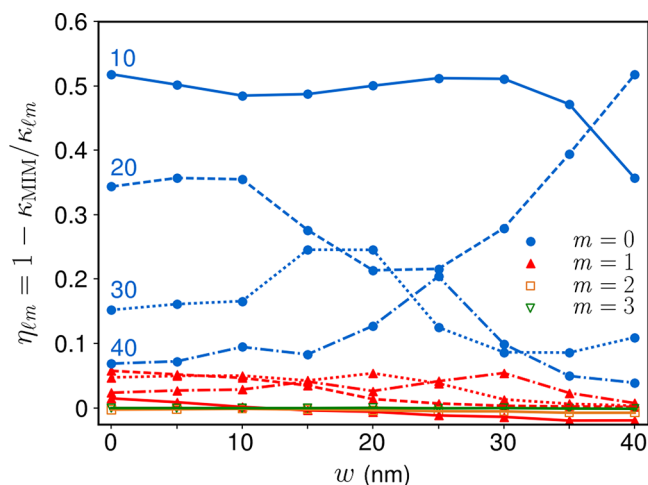


**Figure 4.** Radiation efficiencies  $\eta_{lm}$  of (10), (20), (30), (40), (11), (21), (31), (41), (22), and (33) modes of NPoMs with facet widths from 0 to 40 nm. The (10), (11), (22) and (33) modes are shown as blue, red, orange, and green lines, respectively. The (10) and (11) modes are also further distinguished by solid lines for  $l = 1$ , dashed lines for  $l = 2$ , dotted lines for  $l = 3$ , and dashed-dotted lines for  $l = 4$ .

the (10) modes are the dominant radiative channels of NPoMs, as one would expect. The (10) mode has the highest efficiency for a wide range of  $w$  and is only overtaken by the (20) mode for  $w > 35$  nm. As  $l$  increases, the (10) modes becomes less radiative at  $w = 0$  nm but show complex behaviors near  $w = 20$  nm (due to mode anticrossings). The (11) modes also have non-negligible but small radiation efficiencies below 0.1. In fact, these (11) modes play an essential part in determining the far-field emission, as later shown in Figures 6 and 7. On the other hand, the modes with  $|m| > 1$  are virtually dark, and their

radiation efficiencies are close to zero. We note that the efficiencies of some QNMs, such as the (11) and (22) modes, fall slightly below zero. This is because the MIM plasmonic waveguide represents the NPoM system phenomenologically and, hence, only provides an approximate description.

**Far-Field Emission Profiles.** Having investigated the near-field profiles and eigenfrequencies of individual eigenmodes for NPoMs, it is now straightforward to examine their respective far-field properties. We employ the software code RETOP,<sup>43</sup> which implements a NFFT transformation in dispersive stratified media.<sup>44–46</sup> For each QNM, the electromagnetic fields in the near-field zone,  $(\tilde{\mathbf{E}}_{lm}, \tilde{\mathbf{H}}_{lm})$ , are projected at the same frequency  $\omega_{em}$  to the far-field  $(\tilde{\mathbf{E}}_{lm}^{\text{ff}}, \tilde{\mathbf{H}}_{lm}^{\text{ff}})\exp(ik_{em}R_u)$ , where  $k_{em} = \omega_{em}/c$ , on the upper hemisphere of radius  $R_u$  above the NPoMs. We note that, since the QNMs diverge in space, the NFFTs of all QNMs are evaluated on the same rectangular box surrounding the NPoM (see section S1.2 in the Supporting Information).

The time-average Poynting flux of each QNM,  $\langle S_{lm} \rangle = \text{Re}[(\tilde{\mathbf{E}}_{lm}^{\text{ff}})^* \times \tilde{\mathbf{H}}_{lm}^{\text{ff}}]/2$ , is then evaluated and shown in Figure 5 for spherical ( $w = 0$  nm) and faceted ( $w = 20$  nm) NPoMs. The bright (10) modes show ring-shaped emission patterns with emission peaks near angle  $\theta = 60^\circ$ , while the darker (11) modes show spot-shaped emission, peaked at  $\theta = 0^\circ$ . These results are consistent with those reported previously.<sup>15,16,47</sup> The (22) modes in Figure 5e,h shows far-field emission with four emission lobes, having the same symmetry as their near-field profiles in Figure 2e,h. On the other hand, the (33) mode in Figure 5j shows spot-shaped emission, similar to those of the (11) modes.

Although it is indeed essential to understand how each QNM radiates to the far-field, individual QNMs are rarely excited in isolation. For example, an emitter placed in a NPoM nanocavity couples to a specific collection of the modes, depending on its transition frequency. Hence, accurate far-field analysis of a NPoM must involve reconstructing the collective QNM far-field emission. Here, the coupling coefficients of an electric dipole emitter placed inside a NPoM to its QNMs are evaluated and used to calculate the total far-field emission of the dipole emitter.

For a single emitter with dipole moment  $\boldsymbol{\mu}$  and transition frequency  $\omega_{em}$  placed at position  $\mathbf{r}_{em}$  in close proximity to a plasmonic structure, the electromagnetic fields  $(\mathbf{E}, \mathbf{H})$  radiated by the emitter can be expanded using a small set of QNMs

$$\mathbf{E}(\mathbf{r}) = \sum_i \alpha_i(\mathbf{r}_{em}; \omega_{em}) \tilde{\mathbf{E}}_i(\mathbf{r}) \quad (11)$$

where  $\alpha_i$  is the modal excitation coefficient which can be calculated by<sup>38</sup>

$$\alpha_i(\mathbf{r}_{em}; \omega_{em}) = -\omega \sum_j B_{i,j}^{-1}(\omega_{em}) \boldsymbol{\mu} \cdot \tilde{\mathbf{E}}_j(\mathbf{r}_{em}) \quad (12)$$

$$B_{i,j}(\omega) = \iiint_{\Omega} \{ \tilde{\mathbf{E}}_j \cdot [\omega \boldsymbol{\epsilon}(\mathbf{r}; \omega) - \tilde{\omega}_j \boldsymbol{\epsilon}(\mathbf{r}; \tilde{\omega}_j)] \tilde{\mathbf{E}}_i - \mu_0 \tilde{\mathbf{H}}_j \cdot (\omega - \tilde{\omega}_j) \tilde{\mathbf{H}}_i \} d\mathbf{r}^3 \quad (13)$$

Here, a methylene blue molecule with transition wavelength of  $\lambda_{em} = 660$  nm is chosen as a quantum emitter of choice since it is a typical dye molecule experimentally used inside a NPoM.<sup>11</sup> By placing the emitter with  $\boldsymbol{\mu} = |\boldsymbol{\mu}| \hat{\mathbf{e}}_z$  at position  $x_{em}$  in the gap of a NPoM, its coupling to the NPoM's QNMs in eq 12 can be simplified to

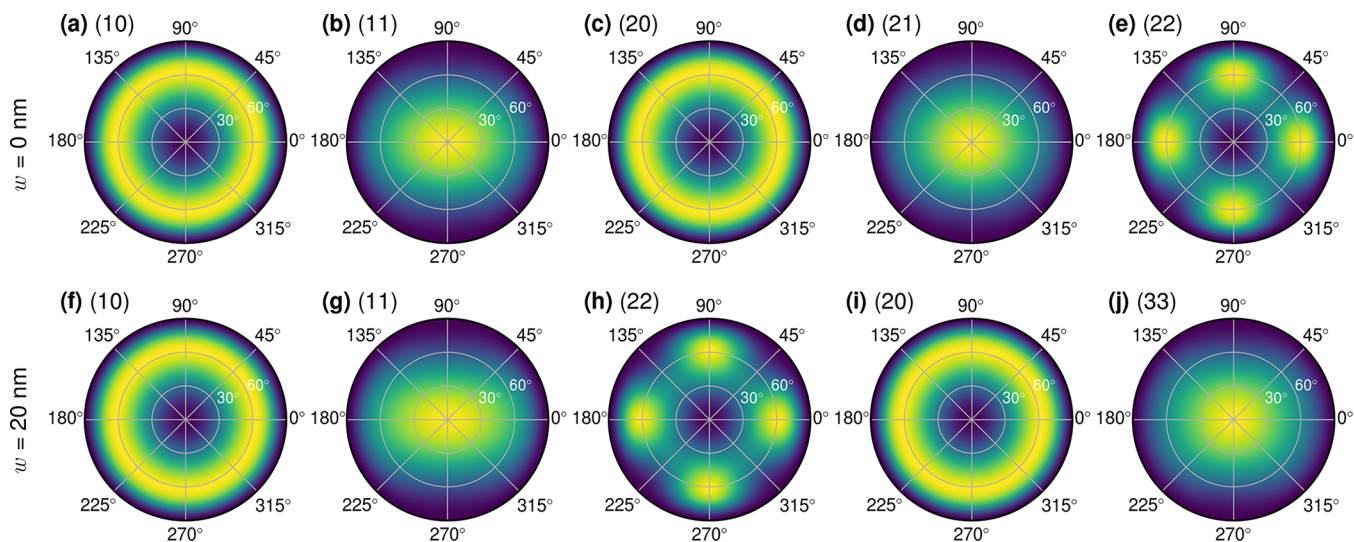


**Figure 5.** Normalized Poynting fluxes  $\langle S_{lm} \rangle$  for the first five QNMs on the upper hemisphere above NPoMs with (a–e)  $w = 0$  nm and (f–j)  $w = 20$  nm.

$$\alpha_{lm}(x_{em}; \omega_{em})/|\mu| = -\omega_{em} \sum_{l'm'} B_{lm,l'm'}^{-1}(\omega_{em}) \tilde{E}_{z,l'm'}(x_{em}) \quad (14)$$

where  $\tilde{E}_{z,l'm'} = \hat{e}_z \cdot \tilde{\mathbf{E}}_{l'm'}$ ,  $\omega_{em} = 2\pi c/\lambda_{em}$ , and only the first 20 QNMs are included in the calculations, as shown in Table S1. The coupling coefficients  $|\alpha_{lm}|$  to different  $(lm)$  modes are shown in Figure 6, as the emitter moves laterally inside the gap along the

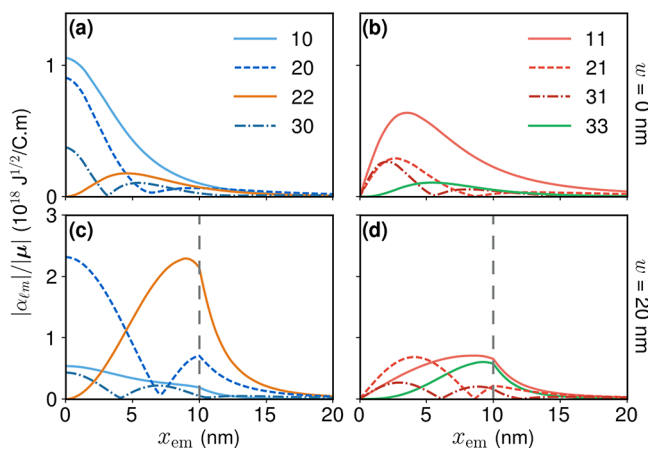


**Figure 6.** QNM coupling coefficient  $\alpha_{lm}$  to an emitter with dipole moment  $\mu$  and transition wavelength  $\lambda_{em} = 660$  nm for different positioning  $x_{em}$  of the emitter. (a, c) First four symmetric and (b, d) first four antisymmetric QNMs of NPoMs with facet widths (a, b)  $w = 0$  nm and (c, d)  $w = 20$  nm. The vertical dashed lines indicate the facet edges.

$x$ -axis. Four QNMs with even  $m$ , Figure 6a,c, are separated in these plots from those with odd  $m$ , Figure 6b,d, as they have symmetric and antisymmetric field profiles across the  $x = 0$  nm plane, respectively. For  $w = 0$  nm, the emitter's resonance lies spectrally close to the (10), (11), and (20), see Figure 3a. In Figure 6a,b, the coupling magnitudes of these three QNMs indeed dominate the coupling with the emitter. The coupling magnitudes of different QNMs change drastically when the facet width increases to  $w = 20$  nm. The emitter instead lies spectrally close to (11), (22), (20), (33), and (21) see Figure 3b, which become the modes coupled to the emitter, as shown

in Figure 6c,d. The relative magnitudes of  $|\alpha_{lm}|$  are crucial in understanding the total far-field emission.

The total far-field emission  $(\tilde{\mathbf{E}}^{\text{ff}}, \tilde{\mathbf{H}}^{\text{ff}})$  from the emitter placed inside a NPoM can then be evaluated by combining the far-field QNM fields  $(\tilde{\mathbf{E}}_{lm}^{\text{ff}}, \tilde{\mathbf{H}}_{lm}^{\text{ff}})$  with complex coupling coefficient  $\alpha_{lm}$

$$(\tilde{\mathbf{E}}^{\text{ff}}(x_{em}; \omega_{em}), \tilde{\mathbf{H}}^{\text{ff}}(x_{em}; \omega_{em})) = \sum_{lm} \alpha_{lm}(x_{em}; \omega_{em}) (\tilde{\mathbf{E}}_{lm}^{\text{ff}}, \tilde{\mathbf{H}}_{lm}^{\text{ff}}) \quad (15)$$

Figure 7 shows the total time-average Poynting flux  $\langle S_{\text{tot}} \rangle = \text{Re}[(\tilde{\mathbf{E}}^{\text{ff}})^* \times \tilde{\mathbf{H}}^{\text{ff}}]/2$  from the emitter placed at lateral positions  $x_{em} = 0, 5, 10,$  and  $15$  nm inside NPoMs with a facet width of either 0 or 20 nm. For  $w = 0$  nm, Figure 7a–d, the emission has a ring-shaped pattern at  $x_{em} = 0$  nm as the emitter is dominantly coupled to the (10) and (20) modes. As the emitter is moved away from the nanocavity center, the emitter couples more efficiently to the (11) mode. The spot-shaped emission from the (11) mode also has a phase variation over the angular coordinate  $\phi$ . At  $x_{em} = 5$  nm, the distorted ring-shaped emission in Figure 7b is the result of this phase variation, giving destructive interference for  $-\pi/2 < \phi < \pi/2$  and constructive interference for  $\pi/2 < \phi < 3\pi/2$  with the ring-shaped emission from the (10) and (20). For larger  $x_{em} \geq 10$  nm, the antisymmetric (11) mode dominates the coupling with the emitter, and the emission becomes an offset spot-shaped pattern. We note that recent experiments show exactly these features.<sup>48</sup>

For the faceted NPoM with facet  $w = 20$  nm, the emission also has a ring-shaped pattern when the emitter is at the center of the cavity since the emitter couples mainly to the (20) mode, see Figure 7e. By moving the emitter within the faceted NPoM to position  $x_{em} = 5$  nm the far-field emission becomes a distorted ring-shaped pattern since the emitter couples more efficiently to the (11) and (21) modes, which is similar to the spherical NPoM in Figure 7b. However, when the emitter moves even closer to the facet edge at  $x_{em} = 10$  nm the far-field emission pattern flips 180°, as shown in Figure 7g. This flip results from changes in the complex coefficients  $\alpha_{lm}$  of different QNMs which instead interfere constructively for  $-\pi/2 < \phi < \pi/2$  and destructively for  $\pi/2 < \phi < 3\pi/2$ . Unlike Figure 7d, the emission at  $x_{em} > 15$  nm in Figure 7h resumes the ring-

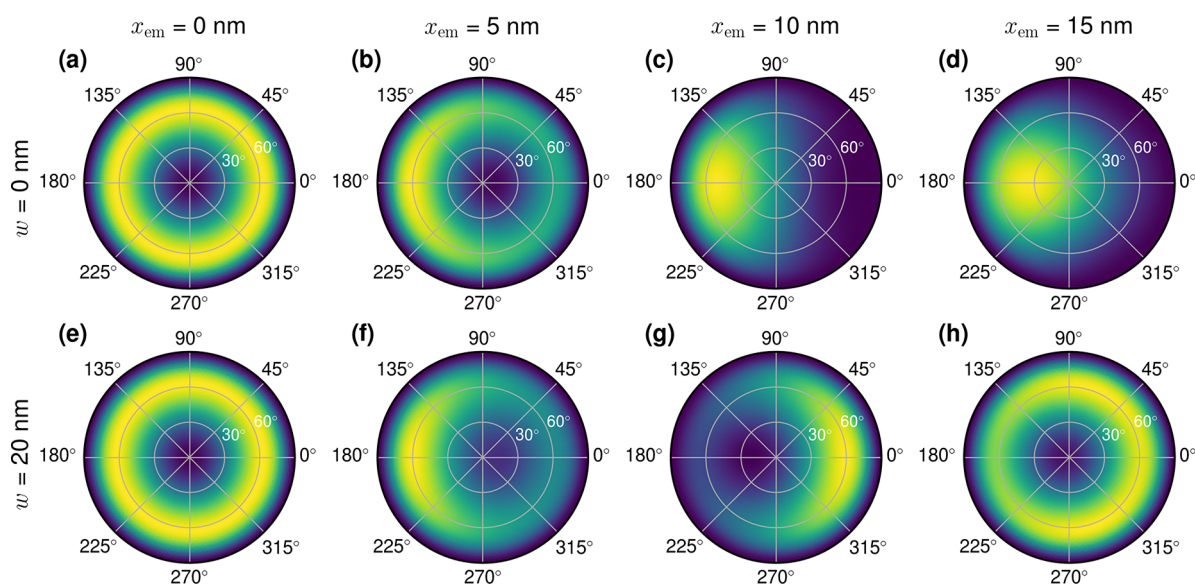


**Figure 7.** Normalized total Poynting fluxes ( $S_{\text{tot}}$ ) of dipole emission emerging in the upper hemisphere above the NPoM, obtained by the QNM method. Single emitters with transition wavelength  $\lambda_{\text{em}} = 660$  nm are placed in the nanogap with facet widths (a–d) 0 nm and (e–h) 20 nm at positions (a, e)  $x_{\text{em}} = 0$  nm, (b, f)  $x_{\text{em}} = 5$  nm, (c, g)  $x_{\text{em}} = 10$  nm, and (d, h)  $x_{\text{em}} = 15$  nm.

shaped pattern for the emitter since the emitter dominantly couples to the symmetric (20) and (22) modes.

The far-field emission profiles in Figure 7 are quantitatively calculated by combining 20 QNMs. In fact, only a small number of dominant QNMs are required to qualitatively capture the main contributions to the far-field profiles. As shown in Figure S7 in the Supporting Information, the (10) and (11) modes are the only dominant QNMs for the 660 nm emitter in the  $w = 0$  nm NPoM. On the other hand, the emission from the faceted NPoM with  $w = 20$  nm requires up to eight QNMs, including the (10), (20), (30), (11), (21), (31), (41), and (51) modes. These results are also confirmed by independent calculations in Figure S8 in the Supporting Information, where the far-field emission is calculated directly from an electric dipole source placed in the NPoMs, effectively exciting all available QNMs. Excellent agreements between Figures 7, S7, and S8 conclude that our calculations involving the first 20 QNMs provide a sufficient quantitative description of the NPoMs.

Figure 7 demonstrates multimodal interaction between the NPoM resonances and the emitter which leads to counter-intuitive far-field emission patterns, depending on the NPoM gap morphology and the emitter's lateral position. These results are essential for understanding experimental measurements involving the emission from emitters placed inside a plasmonic nanocavity and deciphering which plasmon modes they interact with.<sup>48</sup>

## CONCLUSIONS

In recent years, the NPoM geometry (including different shaped nanoparticles such as nanocubes on mirror) has become a prominent nanostructure in nanoplasmonics due to its extreme light confinement properties. However, a comprehensive modal analysis of the structure has not been available, and most current studies infer its resonances from far-field optical scattering. We use the quasinormal mode (QNM) approach to analyze the morphology-dependent plasmonic resonances of the NPoM structure. A collection of bright and dark resonances are revealed, some of which have

not yet been previously reported. A simple and comprehensive nomenclature is introduced based on spherical harmonics which reflects the underlying charge distributions on the nanoparticles. The near-field and far-field optical behaviors of NPoMs with varying facet widths are also reported, which clarifies the inconsistency in previous near-field and far-field analyses. This study also unveils rich and intricate multimodal interactions with a single quantum emitter and has the potential to aid the design of quantum plasmonic experiments, such as quantum computing with DNA-origami-controlled qubits<sup>24</sup> and quantum plasmonic immunoassay sensing.<sup>49</sup>

## ASSOCIATED CONTENT

### Supporting Information

The Supporting Information is available free of charge at <https://pubs.acs.org/doi/10.1021/acsphotonics.9b01445>.

- (1) Numerical methods; (2) Additional QNMs of spherical and faceted NPoMs; (3) Radiation efficiencies of QNMs; (4) Quality factors and mode volumes of QNMs; (5) Dominant QNMs for far-field emission; (6) Direct dipole method for far-field emission (PDF)

## AUTHOR INFORMATION

### Corresponding Authors

Jeremy J. Baumberg – University of Cambridge, Cambridge, United Kingdom; [orcid.org/0000-0002-9606-9488](https://orcid.org/0000-0002-9606-9488); Email: [jjb12@cam.ac.uk](mailto:jjb12@cam.ac.uk)

Ortwin Hess – Imperial College London, London, United Kingdom, and Trinity College Dublin, Dublin 2, Ireland; [orcid.org/0000-0002-6024-0677](https://orcid.org/0000-0002-6024-0677); Email: [ortwin.hess@tcd.ie](mailto:ortwin.hess@tcd.ie)

### Other Authors

Nuttawut Kongsuwan – Imperial College London, London, United Kingdom, and Quantum Technology Foundation of Thailand, Bangkok, Thailand; [orcid.org/0000-0002-8037-3100](https://orcid.org/0000-0002-8037-3100)

Angela Demetriadou – University of Birmingham, Edgbaston, United Kingdom; [orcid.org/0000-0001-7240-597X](https://orcid.org/0000-0001-7240-597X)

Matthew Horton – University of Cambridge, Cambridge, United Kingdom

Rohit Chikkaraddy – University of Cambridge, Cambridge, United Kingdom; [orcid.org/0000-0002-3840-4188](https://orcid.org/0000-0002-3840-4188)

Complete contact information is available at: <https://pubs.acs.org/10.1021/acsphotonics.9b01445>

## Notes

The authors declare no competing financial interest.

## ACKNOWLEDGMENTS

We acknowledge support from the Engineering and Physical Sciences Research Council (EPSRC) UK through Projects EP/L024926/1, EP/L027151/1, EP/N016920/1, and NanoDTC EP/L015978/1. A.D. acknowledges support from the Royal Society URF/R1/180097 and RGF/EA/181038. R.C. acknowledges support from Trinity College Cambridge.

## REFERENCES

- (1) Anger, P.; Bharadwaj, P.; Novotny, L. Enhancement and Quenching of Single-Molecule Fluorescence. *Phys. Rev. Lett.* **2006**, *96*, 113002.
- (2) Savage, K. J.; Hawkeye, M. M.; Esteban, R.; Borisov, A. G.; Aizpurua, J.; Baumberg, J. J. Revealing the quantum regime in tunnelling plasmonics. *Nature* **2012**, *491*, 574–577.
- (3) Prodan, E.; Radloff, C.; Halas, N. J.; Nordlander, P. A hybridization model for the plasmon response of complex nanostructures. *Science* **2003**, *302*, 419–422.
- (4) Zhu, W.; Esteban, R.; Borisov, A. G.; Baumberg, J. J.; Nordlander, P.; Lezec, H. J.; Aizpurua, J.; Crozier, K. B. Quantum mechanical effects in plasmonic structures with subnanometre gaps. *Nat. Commun.* **2016**, *7*, 11495.
- (5) Kinkhabwala, A.; Yu, Z.; Fan, S.; Avlasevich, Y.; Mullen, K.; Moerner, W. E. Large single-molecule fluorescence enhancements produced by a bowtie nanoantenna. *Nat. Photonics* **2009**, *3*, 654–657.
- (6) Chen, H.; Schatz, G. C.; Ratner, M. A. Experimental and theoretical studies of plasmon–molecule interactions. *Rep. Prog. Phys.* **2012**, *75*, 096402.
- (7) Zhang, X.; Chen, Y. L.; Liu, R.-S.; Tsai, D. P. Plasmonic photocatalysis. *Rep. Prog. Phys.* **2013**, *76*, 046401.
- (8) Choo, H.; Kim, M.-K.; Staffaroni, M.; Seok, T. J.; Bokor, J.; Cabrini, S.; Schuck, P. J.; Wu, M. C.; Yablonovitch, E. Nanofocusing in a metal–insulator–metal gap plasmon waveguide with a three-dimensional linear taper. *Nat. Photonics* **2012**, *6*, 838.
- (9) Ciraci, C.; Hill, R.; Mock, J. J.; Urzhumov, Y.; Fernandez-Dominguez, A. I.; Maier, S. A.; Pendry, J. B.; Chilkoti, A.; Smith, D. R. Probing the ultimate limits of plasmonic enhancement. *Science* **2012**, *337*, 1072–1074.
- (10) Mertens, J.; Eiden, A. L.; Sigle, D. O.; Huang, F.; Lombardo, A.; Sun, Z.; Sundaram, R. S.; Colli, A.; Tserkezis, C.; Aizpurua, J.; Milana, S.; Ferrari, A. C.; Baumberg, J. J. Controlling subnanometer gaps in plasmonic dimers using graphene. *Nano Lett.* **2013**, *13*, 5033–5038.
- (11) Chikkaraddy, R.; de Nijs, B.; Benz, F.; Barrow, S. J.; Scherman, O. A.; Rosta, E.; Demetriadou, A.; Fox, P.; Hess, O.; Baumberg, J. J. Single-molecule strong coupling at room temperature in plasmonic nanocavities. *Nature* **2016**, *535*, 127.
- (12) Li, L.; Hutter, T.; Steiner, U.; Mahajan, S. Single molecule SERS and detection of biomolecules with a single gold nanoparticle on a mirror junction. *Analyst* **2013**, *138*, 4574–4578.
- (13) Hensen, M.; Heilpern, T.; Gray, S. K.; Pfeiffer, W. Strong coupling and entanglement of quantum emitters embedded in a nanoantenna-enhanced plasmonic cavity. *ACS Photonics* **2018**, *5*, 240–248.
- (14) Ojambati, O. S.; Chikkaraddy, R.; Deacon, W. D.; Horton, M.; Kos, D.; Turek, V. A.; Keyser, U. F.; Baumberg, J. J. Quantum electrodynamics at room temperature coupling a single vibrating molecule with a plasmonic nanocavity. *Nat. Commun.* **2019**, *10*, 1049.
- (15) Mubeen, S.; Zhang, S.; Kim, N.; Lee, S.; Kramer, S.; Xu, H.; Moskovits, M. Plasmonic properties of gold nanoparticles separated from a gold mirror by an ultrathin oxide. *Nano Lett.* **2012**, *12*, 2088–2094.
- (16) Baumberg, J. J.; Aizpurua, J.; Mikkelsen, M. H.; Smith, D. R. Extreme nanophotonics from ultrathin metallic gaps. *Nat. Mater.* **2019**, *18*, 668–678.
- (17) Sigle, D. O.; Mertens, J.; Herrmann, L. O.; Bowman, R. W.; Ithurria, S.; Dubertret, B.; Shi, Y.; Yang, H. Y.; Tserkezis, C.; Aizpurua, J.; Baumberg, J. J. Monitoring morphological changes in 2D monolayer semiconductors using atom-thick plasmonic nanocavities. *ACS Nano* **2015**, *9*, 825–830.
- (18) Tserkezis, C.; Esteban, R.; Sigle, D. O.; Mertens, J.; Herrmann, L. O.; Baumberg, J. J.; Aizpurua, J. Hybridization of plasmonic antenna and cavity modes: Extreme optics of nanoparticle-on-mirror nanogaps. *Phys. Rev. A: At., Mol., Opt. Phys.* **2015**, *92*, 053811.
- (19) Huh, J.-H.; Lee, J.; Lee, S. Comparative study of plasmonic resonances between the roundest and randomly faceted Au nanoparticles-on-mirror cavities. *ACS Photonics* **2018**, *5*, 413–421.
- (20) Demetriadou, A.; Hamm, J. M.; Luo, Y.; Pendry, J. B.; Baumberg, J. J.; Hess, O. Spatiotemporal dynamics and control of strong coupling in plasmonic nanocavities. *ACS Photonics* **2017**, *4*, 2410–2418.
- (21) Devaraj, V.; Jeong, H.; Kim, C.; Lee, J.-M.; Oh, J.-W. Modifying Plasmonic-Field Enhancement and Resonance Characteristics of Spherical Nanoparticles on Metallic Film: Effects of Faceting Spherical Nanoparticle Morphology. *Coatings* **2019**, *9*, 387.
- (22) Kongsuwan, N.; Demetriadou, A.; Chikkaraddy, R.; Benz, F.; Turek, V. A.; Keyser, U. F.; Baumberg, J. J.; Hess, O. Suppressed quenching and strong-coupling of Purcell-enhanced single-molecule emission in plasmonic nanocavities. *ACS Photonics* **2018**, *5*, 186–191.
- (23) Kongsuwan, N.; Demetriadou, A.; Chikkaraddy, R.; Baumberg, J. J.; Hess, O. Fluorescence enhancement and strong-coupling in faceted plasmonic nanocavities. *EPJ. Appl. Metamat.* **2018**, *5*, 6.
- (24) Chikkaraddy, R.; Turek, V. A.; Kongsuwan, N.; Benz, F.; Carnegie, C.; van de Goor, T.; de Nijs, B.; Demetriadou, A.; Hess, O.; Keyser, U. F.; Baumberg, J. J. Mapping nanoscale hotspots with single-molecule emitters assembled into plasmonic nanocavities using DNA origami. *Nano Lett.* **2018**, *18*, 405–411.
- (25) Nordlander, P.; Prodan, E. Plasmon hybridization in nanoparticles near metallic surfaces. *Nano Lett.* **2004**, *4*, 2209–2213.
- (26) Faggiani, R.; Yang, J.; Lalanne, P. Quenching, Plasmonic, and Radiative Decays in Nanogap Emitting Devices. *ACS Photonics* **2015**, *2*, 1739–1744.
- (27) Yan, W.; Faggiani, R.; Lalanne, P. Rigorous modal analysis of plasmonic nanoresonators. *Phys. Rev. B: Condens. Matter Mater. Phys.* **2018**, *97*, 205422.
- (28) Lombardi, A.; Demetriadou, A.; Weller, L.; Andrae, P.; Benz, F.; Chikkaraddy, R.; Aizpurua, J.; Baumberg, J. J. Anomalous spectral shift of near- and far-field plasmonic resonances in nanogaps. *ACS Photonics* **2016**, *3*, 471–477.
- (29) Benz, F.; Chikkaraddy, R.; Salmon, A.; Ohadi, H.; De Nijs, B.; Mertens, J.; Carnegie, C.; Bowman, R. W.; Baumberg, J. J. SERS of individual nanoparticles on a mirror: size does matter, but so does shape. *J. Phys. Chem. Lett.* **2016**, *7*, 2264–2269.
- (30) Lalanne, P.; Yan, W.; Vynck, K.; Sauvan, C.; Hugonin, J.-P. Light interaction with photonic and plasmonic resonances. *Laser Photonics Rev.* **2018**, *12*, 1700113.
- (31) Ching, E.; Leung, P.; van den Brink, A. M.; Suen, W.; Tong, S.; Young, K. Quasinormal-mode expansion for waves in open systems. *Rev. Mod. Phys.* **1998**, *70*, 1545.
- (32) Kokkotas, K. D.; Schmidt, B. G. Quasi-normal modes of stars and black holes. *Living Rev. Relativ.* **1999**, *2*, 2.

- (33) Ge, R. C.; Hughes, S. Design of an efficient single photon source from a metallic nanorod dimer: a quasi-normal mode finite-difference time-domain approach. *Opt. Lett.* **2014**, *39*, 4235–4238.
- (34) Kristensen, P. T.; Hughes, S. Modes and mode volumes of leaky optical cavities and plasmonic nanoresonators. *ACS Photonics* **2014**, *1*, 2–10.
- (35) Bai, Q.; Perrin, M.; Sauvan, C.; Hugonin, J.-P.; Lalanne, P. Efficient and intuitive method for the analysis of light scattering by a resonant nanostructure. *Opt. Express* **2013**, *21*, 27371–27382.
- (36) Powell, D. A. Resonant dynamics of arbitrarily shaped meta-atoms. *Phys. Rev. B: Condens. Matter Mater. Phys.* **2014**, *90*, 075108.
- (37) Zheng, X.; Valev, V. K.; Verellen, N.; Volskiy, V.; Herrmann, L. O.; Van Dorpe, P.; Baumberg, J. J.; Vandenbosch, G. A.; Moschchalkov, V. Implementation of the natural mode analysis for nanotopologies using a volumetric method of moments (V-MoM) algorithm. *IEEE Photonics J.* **2014**, *6*, 1–13.
- (38) Sauvan, C.; Hugonin, J. P.; Maksymov, I. S.; Lalanne, P. Theory of the Spontaneous Optical Emission of Nanosize Photonic and Plasmon Resonators. *Phys. Rev. Lett.* **2013**, *110*, 237401.
- (39) Bohren, C. F.; Huffman, D. R. *Absorption and Scattering of Light by Small Particles*; John Wiley & Sons, Inc, 1998.
- (40) Low, F. E.; Wald, M. Classical Field Theory: Electromagnetism and Gravitation. *Phys. Today* **1997**, *50*, 68.
- (41) Mertens, J.; Demetriadou, A.; Bowman, R. W.; Benz, F.; Kleemann, M. E.; Tserkezis, C.; Shi, Y.; Yang, H. Y.; Hess, O.; Aizpurua, J.; Baumberg, J. J. Tracking Optical Welding through Groove Modes in Plasmonic Nanocavities. *Nano Lett.* **2016**, *16*, 5605–5611.
- (42) Maier, S. A. *Plasmonics: Fundamentals and Applications*; Springer Science & Business Media, 2007.
- (43) Yang, J.; Hugonin, J.-P.; Lalanne, P. Near-to-Far Field Transformations for Radiative and Guided Waves. *ACS Photonics* **2016**, *3*, 395–402.
- (44) Balanis, C. A. *Antenna Theory Analysis and Design*; Wiley, 2016.
- (45) Demarest, K.; Huang, Z.; Plumb, R. An FDTD near-to far-zone transformation for scatterers buried in stratified grounds. *IEEE Trans. Antennas Propag.* **1996**, *44*, 1150–1157.
- (46) Pors, A.; Bozhevolnyi, S. I. Quantum emitters near layered plasmonic nanostructures: Decay rate contributions. *ACS Photonics* **2015**, *2*, 228–236.
- (47) Chikkaraddy, R.; Zheng, X.; Benz, F.; Brooks, L. J.; De Nijs, B.; Carnegie, C.; Kleemann, M.-E.; Mertens, J.; Bowman, R. W.; Vandenbosch, G. A.; Moshchalkov, V. V.; Baumberg, J. J. How ultranarrow gap symmetries control plasmonic nanocavity modes: from cubes to spheres in the nanoparticle-on-mirror. *ACS Photonics* **2017**, *4*, 469–475.
- (48) Horton, M. J.; Ojambati, O. S.; Chikkaraddy, R.; Deacon, W. M.; Kongsuwan, N.; Demetriadou, A.; Hess, O.; Baumberg, J. J. Nanoscopy through a plasmonic nano-lens. *Proc. Natl. Acad. Sci. U. S. A.* **2020**, 201914713.
- (49) Kongsuwan, N.; Xiong, X.; Bai, P.; You, J.-B.; Png, C. E.; Wu, L.; Hess, O. Quantum Plasmonic Immunoassay Sensing. *Nano Lett.* **2019**, *19*, 5853–5861.